pulses. These isotropic changes in R correspond to a temperature change of a fraction of a Kelvin over the probing time interval.

We also observe these AMR symmetries in higher-temperature measurements. However, the AMR changes sign between the higher- and lower-temperature data, as seen when comparing the transverse resistance signals in Figs. 2 and 3 with the corresponding measurements in the first row of Fig. 4. The change in sign of the AMR is further confirmed in fig. S3 (see also the supplementary text), where the measured temperature dependence of AMR is shown and compared to calculations. From this comparison, we can infer the preferred AFM spin-axis direction for the given writing current direction. The experimental and theoretical AMR signs match if the AFM spin axis aligns perpendicular to the writing current. This is consistent with the predicted direction of the spin-orbit current-induced fields and with the XMLD-PEEM results. Measurements at high magnetic fields shown in fig. S3 (see also supplementary text) give further confirmation that the AFM spin axis aligns perpendicular to the setting current pulses. These measurements also highlight that our AFM memory can be read and written by the staggered current-induced fields and the memory state retained even in the presence of strong magnetic fields.

The staggered current-induced fields that we observe are not unique to CuMnAs. The high–Néel temperature AFM Mn_2Au (*37*) is another example in which the spin sublattices form inversion partners and where theory predicts large field-like torques of the form $dM_{A,B}/dt \sim M_{A,B} \times p_{A,B}$ with $p_A = -p_B$ (*19*). From our microscopic density-functional calculations, we obtain a current-induced field of around 20 Oe per 10^7 A cm^{-2} in Mn_2Au, which, combined with its higher conductivity, may make this a favorable system for observing current-driven AFM switching. AFMs that do not possess these specific symmetries can in principle be switched by injecting a spin current into the AFM from a spin-orbit–coupled nonmagnetic (NM) layer using an applied in-plane electrical current via the spin Hall effect, generating the antidamping-like torque $dM_{A,B}/dt \sim M_{A,B} \times (M_{A,B} \times p)$ (*19*). The same type of torque can be generated by the spin-orbit Berry-curvature mechanism acting at the inversion-asymmetric AFM/NM interface or in bare AFM crystals with globally noncentrosymmetric unit cells like CuMnSb (*19*). Our experiments in CuMnAs, combined with the prospect of other realizations of these relativistic nonequilibrium phenomena in AFMs, indicate that AFMs are now ready to join the rapidly developing fields of basic and applied spintronics, enriching this area of solid-state physics and microelectronics by the range of unique characteristics of AFMs.

REFERENCES AND NOTES

1. C. Chappert, A. Fert, F. N. Van Dau, *Nat. Mater.* **6**, 813–823 (2007).
2. A. V. Kimel, A. Kirilyuk, A. Tsvetkov, R. V. Pisarev, T. Rasing, *Nature* **429**, 850–853 (2004).
3. M. Fiebig *et al.*, *J. Phys. D Appl. Phys.* **41**, 164005 (2008).
4. T. Yamaoka, *J. Phys. Soc. Jpn.* **36**, 445–450 (1974).
5. W. Zhang *et al.*, *Phys. Rev. Lett.* **113**, 196602 (2014).
6. T. Jungwirth *et al.*, *Phys. Rev. B* **83**, 035321 (2011).
7. F. Máca *et al.*, *J. Magn. Magn. Mater.* **324**, 1606–1612 (2012).
8. L. Néel, www.nobelprize.org/nobel_prizes/physics/laureates/1970/neel-lecture.pdf.
9. R. Y. Umetsu, A. Sakuma, K. Fukamichi, *Appl. Phys. Lett.* **89**, 052504 (2006).
10. J. Daughton, *Thin Solid Films* **216**, 162–168 (1992).
11. A. B. Shick, S. Khmelevskyi, O. N. Mryasov, J. Wunderlich, T. Jungwirth, *Phys. Rev. B* **81**, 212409 (2010).
12. B. G. Park *et al.*, *Nat. Mater.* **10**, 347–351 (2011).
13. Y. Y. Wang *et al.*, *Phys. Rev. Lett.* **109**, 137201 (2012).
14. X. Marti *et al.*, *Nat. Mater.* **13**, 367–374 (2014).
15. I. Fina *et al.*, *Nat. Commun.* **5**, 4671 (2014).
16. T. Moriyama *et al.*, *Appl. Phys. Lett.* **107**, 122403 (2015).
17. D. Kriegner *et al.*, http://arxiv.org/abs/1508.04877.
18. H. V. Gomonay, V. M. Loktev, *Phys. Rev. B* **81**, 144427 (2010).
19. J. Železný *et al.*, *Phys. Rev. Lett.* **113**, 157201 (2014).
20. P. Wadley *et al.*, *Nat. Commun.* **4**, 2322 (2013).
21. B. Bernevig, O. Vafek, *Phys. Rev. B* **72**, 033203 (2005).
22. A. Chernyshov *et al.*, *Nat. Phys.* **5**, 656–659 (2009).
23. M. Endo, F. Matsukura, H. Ohno, *Appl. Phys. Lett.* **97**, 222501 (2010).
24. D. Fang *et al.*, *Nat. Nanotechnol.* **6**, 413–417 (2011).
25. A. Manchon, S. Zhang, *Phys. Rev. B* **78**, 212405 (2008).
26. I. M. Miron *et al.*, *Nat. Mater.* **9**, 230–234 (2010).
27. U. H. Pi *et al.*, *Appl. Phys. Lett.* **97**, 162507 (2010).
28. T. Suzuki *et al.*, *Appl. Phys. Lett.* **98**, 142505 (2011).
29. I. M. Miron *et al.*, *Nature* **476**, 189–193 (2011).
30. A. Y. Silov *et al.*, *Appl. Phys. Lett.* **85**, 5929 (2004).
31. Y. K. Kato, R. C. Myers, A. C. Gossard, D. D. Awschalom, *Phys. Rev. Lett.* **93**, 176601 (2004).
32. S. D. Ganichev *et al.*, http://arxiv.org/abs/cond-mat/0403641 (2004).
33. J. Wunderlich, B. Kaestner, J. Sinova, T. Jungwirth, http://arxiv.org/abs/cond-mat/0410295v1 (2004).
34. J. Wunderlich, B. Kaestner, J. Sinova, T. Jungwirth, *Phys. Rev. Lett.* **94**, 047204 (2005).
35. F. Freimuth, S. Blügel, Y. Mokrousov, *Phys. Rev. B* **90**, 174423 (2014).
36. V. Hills *et al.*, *J. Appl. Phys.* **117**, 172608 (2015).
37. V. M. T. S. Barthem, C. V. Colin, H. Mayaffre, M.-H. Julien, D. Givord, *Nat. Commun.* **4**, 2892 (2013).

ACKNOWLEDGMENTS

We acknowledge support from the European Union (EU) European Research Council Advanced (grant 268066); the Ministry of Education of the Czech Republic (grant LM2011026); the Grant Agency of the Czech Republic (grant 14-37427); the UK Engineering and Physical Sciences Research Council (grant EP/K027808/1); the EU 7th Framework Programme (grant REGPOT-CT-2013-316014 and FP7-People-2012-ITN-316657); HGF Programme VH-NG 513 and Deutsche Forschungsgemeinschaft SPP 1568; supercomputing resources at Jülich Supercomputing Centre and RWTH Aachen University; and Diamond Light Source for the allocation of beamtime under proposal number SI-12504. We thank C. Nelson for providing the scanning transmission electron microscopy measurement.

SUPPLEMENTARY MATERIALS

www.sciencemag.org/content/351/6273/587/suppl/DC1
Supplementary Text
Figs. S1 to S3
References (*38*, *39*)

11 March 2015; accepted 4 January 2016
Published online 14 January 2016
10.1126/science.aab1031

ICE SHEETS

Holocene deceleration of the Greenland Ice Sheet

Joseph A. MacGregor,[1]* William T. Colgan,[2]† Mark A. Fahnestock,[3] Mathieu Morlighem,[4] Ginny A. Catania,[1,5] John D. Paden,[6] S. Prasad Gogineni[6]

Recent peripheral thinning of the Greenland Ice Sheet is partly offset by interior thickening and is overprinted on its poorly constrained Holocene evolution. On the basis of the ice sheet's radiostratigraphy, ice flow in its interior is slower now than the average speed over the past nine millennia. Generally higher Holocene accumulation rates relative to modern estimates can only partially explain this millennial-scale deceleration. The ice sheet's dynamic response to the decreasing proportion of softer ice from the last glacial period and the deglacial collapse of the ice bridge across Nares Strait also contributed to this pattern. Thus, recent interior thickening of the Greenland Ice Sheet is partly an ongoing dynamic response to the last deglaciation that is large enough to affect interpretation of its mass balance from altimetry.

The dynamics of the Greenland Ice Sheet (GrIS) are coupled intimately with the surrounding ocean (*1*), overlying atmosphere (*2*), and underlying lithosphere (*3*). The large range of time scales spanned by these interactions and the GrIS's own internal dynamics (*4*) challenge our ability to predict GrIS evolution within the context of ongoing Holocene climate change (*5*, *6*).

Despite a rapidly warming climate (*6*), recent dramatic changes in ocean-terminating outlet glaciers along the margin of the GrIS (*7*–*9*), its vulnerability to further oceanic erosion (*10*), and a sustained negative total mass balance (*11*–*13*), more than half of the GrIS interior is presently thickening (*8*, *14*–*16*), and a portion of its southwestern margin is decelerating (*17*). Climate histories reconstructed from ice cores show that the GrIS persisted even when atmospheric temperatures were higher by several degrees Celsius (*18*) and insolation forcing was larger than at present (*19*). Reconciling these observations is critical to

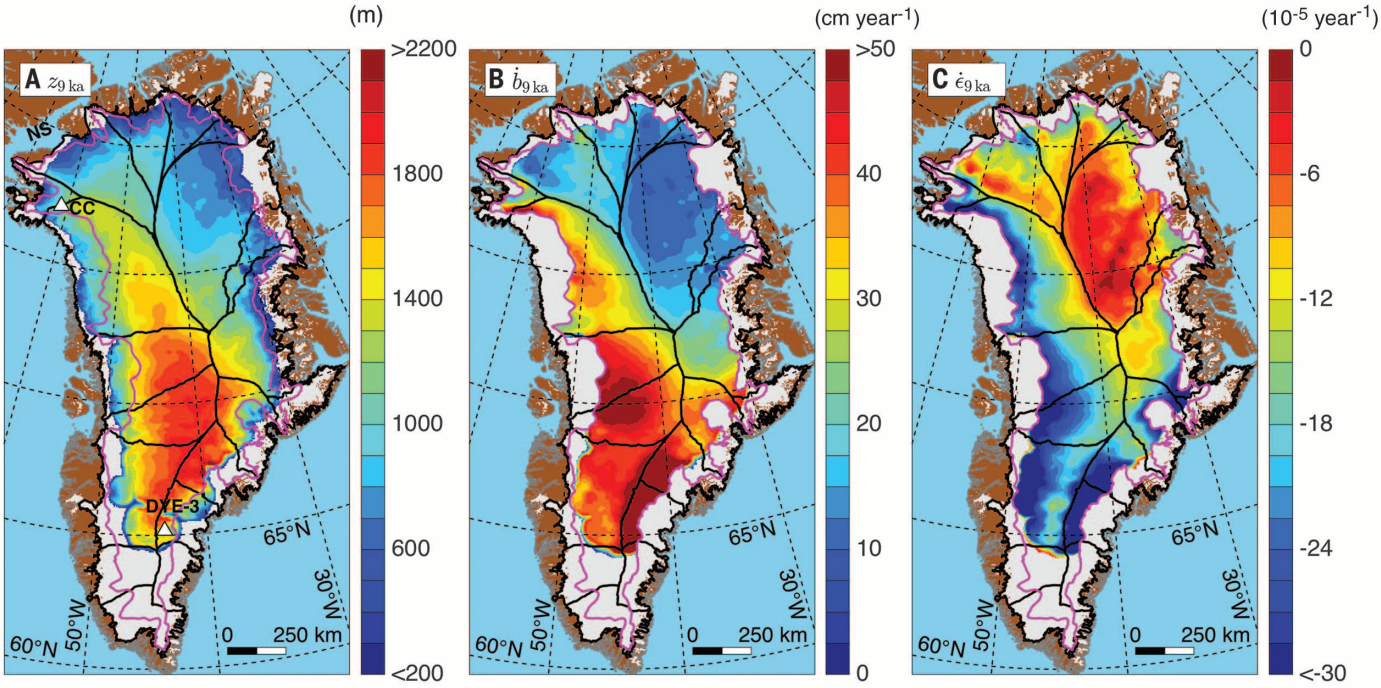

Fig. 1. Constraints on the Holocene-averaged balance ice flux across the GrIS from dated radiostratigraphy. (**A**) Ice-equivalent depth of the 9-ka isochrone (z_{9ka}) [determined as in (*21*)]. Black lines denote major ice-drainage basins (*36*). NS, Nares Strait. White triangles denote Camp Century (CC) and DYE-3 ice core sites. The magenta line represents the outer limit of reliable 1D modeling of depth-age relations to 9 ka (fig. S4). (**B**) Mean ice-equivalent accumulation rate over the past 9000 years ($\dot{b}_{9ka}$). (**C**) Mean vertical strain rate within the 9- to 0-ka portion of the ice column ($\dot{\epsilon}_{9ka}$).

predicting the future of the GrIS amid ongoing climate change.

The internal stratigraphy of an ice sheet, as observed by ice-penetrating radar, provides a valuable constraint upon its history (*3*, *20*). This radiostratigraphy records the spatial variation of an ice sheet's response to the combination of both external forcings and its internal dynamics. Here we use a dated radiostratigraphy for the whole of the GrIS (*21*) to calculate the ice sheet's balance velocity during the last three quarters of the Holocene epoch [9 to 0 thousand years ago (ka)].

Balance velocities represent the pattern of depth-averaged ice flow (*22*). Instead of calculating the balance velocity for the entire ice column, we restrict our analysis to the portion of the ice sheet between the subaerial ice surface and the depth of the 9-ka isochrone (Fig. 1A and fig. S1). This approach avoids the complexity inherent to the interpretation of deeper radiostratigraphy, which is more likely to have experienced substantial horizontal shear and nonsteady flow.

[1]Institute for Geophysics, The University of Texas at Austin, Austin, TX 78758, USA. [2]Geological Survey of Denmark and Greenland, Copenhagen DK-1350, Denmark. [3]Geophysical Institute, University of Alaska Fairbanks, Fairbanks, AK 99775, USA. [4]Department of Earth System Science, University of California, Irvine, Irvine, CA 92697, USA. [5]Department of Geological Sciences, The University of Texas at Austin, Austin, TX 78712, USA. [6]Center for Remote Sensing of Ice Sheets, The University of Kansas, Lawrence, KS 66045, USA.
***Corresponding author. E-mail: joemac@ig.utexas.edu** †Present address: Department of Earth and Space Science and Engineering, York University, Toronto, Ontario M3J 1P3, Canada.

The input ice flux during the Holocene is estimated using the mean accumulation rate over the past 9000 years from one-dimensional (1D) modeling of the depth-age relation of dated reflections (Fig. 1B and figs. S2 and S3) (*3*), instead of using a compilation or model of modern accumulation rates. During this period, the accumulation-rate history of Greenland's interior was stable across millennial time scales (*23*), except more than 7 ka in the northwest region, where it was lower (*24*). Holocene thinning of the GrIS (*5*) would have increased vertical strain rates, but this effect is small compared with the relative change in accumulation rate between our period of interest and modern values (fig. S8).

When calculating a full-thickness balance velocity, the basal mass balance is assumed to be negligible. In our analysis, the equivalent quantity is the vertical velocity at the depth of the 9-ka isochrone, which is rarely negligible but readily estimated using the same 1D models. Because the ratio between the Holocene-averaged balance and surface speeds is often close to unity (figs. S5 and S6), we can directly compare maps of Holocene-averaged and modern surface velocity. These 1D models and the balance velocity are evaluated only in the ice-sheet interior, where the paths of the particles that form these Holocene-aged reflections are less likely to have been distorted drastically by horizontal gradients in ice flow (*25*) (fig. S4).

We find that most of the GrIS interior (95%) is slower now than it was, on average, during the Holocene (Fig. 2). Even near the central ice divide, where the absolute decrease in surface speed is low, the relative decrease in speed is also large (>50%). Considering modeling uncertainty, >87% of the ice-sheet interior has decelerated significantly (fig. S7). Generally higher accumulation rates during this period can explain this pattern only in northeastern Greenland (Fig. 3A and figs. S7 and S8), indicating that the inferred deceleration includes a dynamic component elsewhere. This widespread Holocene deceleration of the GrIS suggests that its dynamic response to the last deglaciation continues to propagate throughout the ice sheet.

The millennial-scale evolution of GrIS rheology can partly explain this response. Ice deposited during the last glacial period (LGP) is approximately three times less viscous ("softer") than ice deposited during the Holocene (*26*). To explain observations of subtle thickening (~1 cm year^{-1}) at DYE-3, Reeh (*4*) hypothesized that, as softer LGP ice is buried by stiffer Holocene ice, the GrIS interior will thicken (hereafter referred to as "Reeh thickening"). Reeh thickening is distinct from that induced by increased accumulation rate, decreased rate of firn densification, post-LGP isostatic adjustment, or horizontal deceleration due to other poorly constrained mechanisms (e.g., increasing basal friction). By continuity, it follows that this transient viscosity change would also have caused the GrIS interior to decelerate after deglaciation.

We assess the modern ice-sheet–wide deceleration associated with the LGP-Holocene viscosity contrast by modeling this deceleration at the GrIS surface with a second, independent 1D ice-flow model. This model includes a 3:1

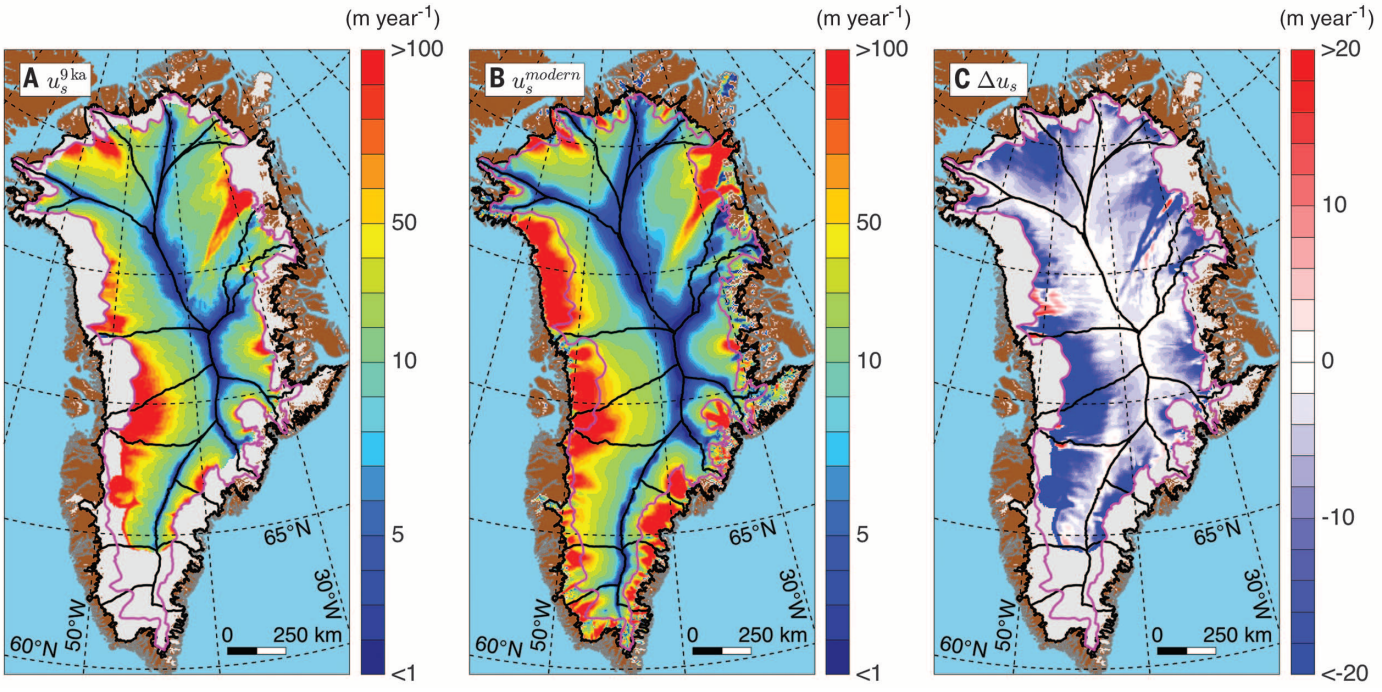

Fig. 2. Holocene-averaged and modern surface speed across the GrIS. (**A**) Holocene-averaged surface speed u_s^{9ka} (i.e., Holocene balance speed divided by shape factor) (fig. S5B). (**B**) Composite surface speed, u_s^{modern}, from 1995–2013 (*37*). (**C**) Change in surface speed between the present and the Holocene average ($\Delta u_s = u_s^{modern} - u_s^{9ka}$).

viscosity contrast (*26*) at the present depth of the beginning of the Holocene (11.7 ka) (*21*) and is consistent with modern surface velocity and ice temperature estimated by a higher-order ice-sheet model (*27*). The modeled horizontal deceleration rate (Fig. 3B), resulting from the downward advection of the LGP-Holocene transition (fig. S9), is most comparable to that which we observed in southern Greenland (south of 68°N) (Fig. 3C). There, Holocene-averaged accumulation rates are relatively high (fig. S8), so the rate of burial of LGP ice by Holocene ice is higher, the LGP-Holocene transition is deeper, and its associated viscosity contrast exerts a greater influence upon ice flow. Holocene-averaged accumulation rates in the southern GrIS are higher than modern values only in a narrow region along the central ice divide and are lower on the flanks (fig. S8), further supporting the notion of a dynamic component to the inferred deceleration (Fig. 3A).

Corroborating and expanding upon Reeh's original hypothesis, we suggest that downward advection of the LGP-Holocene transition partly explains the subtle deceleration we infer in the interior of the southern GrIS. The dynamic consequences of this effect are predicted to have increased nonlinearly within the GrIS interior during the Holocene and to continue for tens of millennia (*4*).

The rheological evolution of the GrIS occurred in conjunction with substantial peripheral changes during the last deglaciation, as it retreated from the continental shelf, with subsequent effects on the interior. In particular, during the LGP, the northwestern sector of the GrIS was connected to the Innuitian Ice Sheet across Nares Strait (*28*). After the last deglaciation, the GrIS thinned rapidly at Camp Century (*5*). This thinning was attributed to the collapse of the Nares Strait ice bridge ~10 ka (*5*, *29*), and residual thinning may be ongoing (*30*). The Holocene-averaged flow of this sector of the ice sheet was significantly faster than at present (Fig. 2C), and its subsequent dynamic deceleration is at least an order of magnitude greater than can be attributed to the LGP-Holocene viscosity contrast (Fig. 3). This sector's Holocene-averaged accumulation rate was significantly lower than at present (fig. S8) (*24*), which also suggests that substantial dynamic thinning occurred there. Together, these patterns indicate that faster ice flow in northwestern Greenland during the Holocene included a dynamic response to ice-bridge collapse.

The Holocene deceleration of the northeastern GrIS is similar in magnitude to that of the northwest region, but it is more likely related to higher Holocene-averaged accumulation rates than to modern rates (Fig. 3A and fig. S8D). Accumulation rates in this region are low (<20 cm year^{-1}) (Fig. 1B), so the dynamic component of this deceleration is harder to constrain, given the difference between Holocene-averaged and modern patterns of accumulation rates. Substantial burial of LGP ice by Holocene ice has yet to occur there (Fig. 1A), so the predicted deceleration due to the LGP-Holocene viscosity contrast is negligible (Fig. 3B). This sector is partially grounded below sea level (*10*) and recently experienced rapid grounding-line retreat (*9*). This vulnerable configuration probably existed throughout the Holocene and may have produced repeated rapid dynamic changes that we cannot resolve from a multimillennial mean balance velocity.

Assuming conservation of mass, the modern horizontal deceleration rates we infer are proportional to dynamically induced rates of ice-sheet thickening. Multiyear to multidecadal altimetric and mass balance observations from multiple platforms show that the interiors of most major GrIS drainage basins have thickened, particularly in southwestern and northeastern Greenland (*8*, *11*, *14*–*16*, *30*). These changes could be related to a warming-induced increase in precipitation in the interior (*31*) or decadal-scale variability in accumulation rate (*32*), but there is low confidence in these possibilities (*33*). We propose that this thickening is partly due to ongoing subtle deceleration of the GrIS interior and transient multimillennial-scale processes that are not directly related to modern climate. The region of greatest observed thickening is the southern GrIS interior (south of 70°N) (Fig. 3C), where inferred and modeled rates of horizontal deceleration are also best correlated (Fig. 3C), strongly suggesting that non-negligible Reeh thickening is occurring there.

Gravimetric and input-output–method estimates of ice-sheet mass balance should be less sensitive to Reeh thickening, which may explain the good agreement between these two methods for the GrIS (*11*, *34*). Analyses of altimetric observations of the southern GrIS that do not account for Reeh thickening risk misattribution of

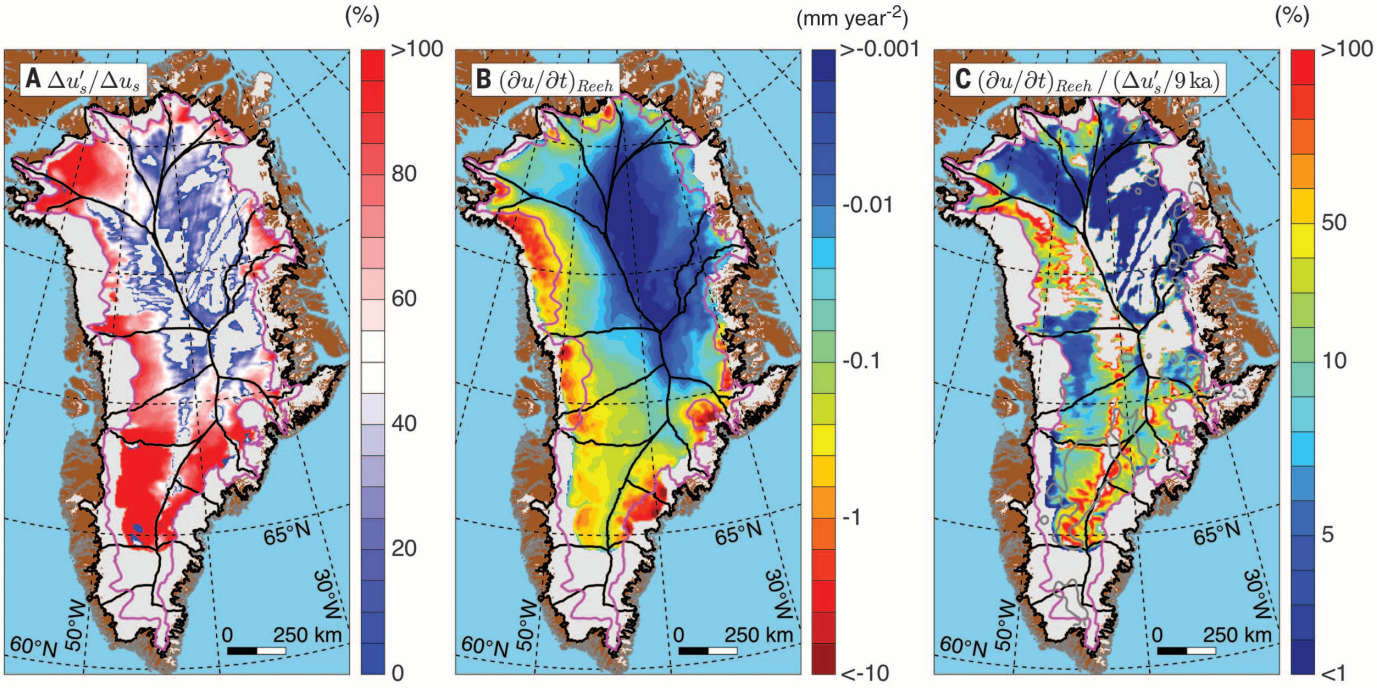

Fig. 3. Dynamic Holocene deceleration of the GrIS. (**A**) Relative contribution of ice dynamics to change in surface speed ($\Delta u'_s/\Delta u_s$). Gaps in coverage are due to positive $\Delta u'_s$ values. (**B**) Modeled horizontal deceleration rate due to the LGP-Holocene viscosity contrast[$(\partial u/\partial t)_{Reeh}$] over the past 1000 years, where $z_{11.7ka}$ is available (*21*). (**C**) Ratio of modeled to inferred dynamic deceleration rate [$(\partial u/\partial t)_{Reeh}/(\Delta u'_s/9\,\mathrm{ka})$]. Gray contours outline regions where the mean 2003–2009 thickening rate was >10 cm year^{-1} (*16*).

long-term dynamic thickening as overestimated accumulation rate and, hence, also as overestimated total ice-sheet mass balance. Indeed, in a recent intercomparison study, laser altimetry estimates of GrIS mass balance exceed those of the other two methods (*11*).

Our results demonstrate that the GrIS's multimillennial-scale response to the last deglaciation is elucidated by its radiostratigraphy and that this response continues to influence its present dynamics. Whereas recent decadal–to–centennial-scale climate forcings are likely the primary cause of the GrIS's present negative mass balance (*13*), this more recent response is overprinted on the ice sheet's millennial-scale evolution. For southern Greenland in particular, ignoring this long-term dynamic signal risks underestimating recent mass loss when invoking the common assumption of reference-period steady state (*35*). Separately, the Holocene deceleration of the northwestern sector of the GrIS is further evidence of both the sensitivity and long-term memory of the ice sheet to evolving boundary conditions.

REFERENCES AND NOTES

1. I. Joughin, R. B. Alley, D. M. Holland, *Science* **338**, 1172–1176 (2012).
2. L. C. Andrews *et al.*, *Nature* **514**, 80–83 (2014).
3. M. Fahnestock, W. Abdalati, I. Joughin, J. Brozena, P. Gogineni, *Science* **294**, 2338–2342 (2001).
4. N. Reeh, *Nature* **317**, 797–799 (1985).
5. B. M. Vinther *et al.*, *Nature* **461**, 385–388 (2009).
6. S. A. Marcott, J. D. Shakun, P. U. Clark, A. C. Mix, *Science* **339**, 1198–1201 (2013).
7. T. Moon, I. Joughin, B. Smith, I. Howat, *Science* **336**, 576–578 (2012).
8. B. M. Csatho *et al.*, *Proc. Natl. Acad. Sci. U.S.A.* **111**, 18478–18483 (2014).
9. J. Mouginot *et al.*, *Science* **350**, 1357–1361 (2015).
10. M. Morlighem, E. Rignot, J. Mouginot, H. Seroussi, E. Larour, *Nat. Geosci.* **7**, 418–422 (2014).
11. A. Shepherd *et al.*, *Science* **338**, 1183–1189 (2012).
12. J. E. Box, W. Colgan, *J. Clim.* **26**, 6990–7002 (2013).
13. K. K. Kjeldsen *et al.*, *Nature* **528**, 396–400 (2015).
14. R. Thomas *et al.*, *Science* **289**, 426–428 (2000).
15. O. M. Johannessen, K. Khvorostovsky, M. W. Miles, L. P. Bobylev, *Science* **310**, 1013–1016 (2005).
16. T. Schenk, B. Csáthó, *IEEE Trans. Geosci. Rem. Sens.* **50**, 3302–3316 (2012).
17. A. J. Tedstone *et al.*, *Nature* **526**, 692–695 (2015).
18. NEEM community members, *Nature* **493**, 489–494 (2013).
19. W. J. van de Berg, M. van den Broeke, J. Ettema, E. van Meijgaard, F. Kaspar, *Nat. Geosci.* **4**, 679–683 (2011).
20. I. M. Whillans, *Nature* **264**, 152–155 (1976).
21. J. A. MacGregor *et al.*, *J. Geophys. Res. Earth Surf.* **120**, 212–241 (2015).
22. A. M. Le Brocq, A. J. Payne, M. J. Siegert, *Comput. Geosci.* **32**, 1780–1795 (2006).
23. D. A. Meese *et al.*, *Science* **266**, 1680–1682 (1994).
24. S. O. Rasmussen *et al.*, *Clim. Past* **9**, 2713–2730 (2013).
25. E. D. Waddington, T. A. Neumann, M. R. Koutnik, H.-P. Marshall, D. L. Morse, *J. Glaciol.* **53**, 694–712 (2007).
26. W. S. B. Paterson, *Cold Reg. Sci. Technol.* **20**, 75–98 (1991).
27. H. Seroussi *et al.*, *J. Glaciol.* **59**, 1024–1034 (2013).
28. J. England *et al.*, *Quat. Sci. Rev.* **25**, 689–703 (2006).
29. M. Zreda, J. England, F. Phillips, D. Elmore, P. Sharma, *Nature* **398**, 139–142 (1999).
30. W. S. B. Paterson, N. Reeh, *Nature* **414**, 60–62 (2001).
31. J. Ettema *et al.*, *Geophys. Res. Lett.* **36**, L12501 (2009).
32. J. R. McConnell *et al.*, *Nature* **406**, 877–879 (2000).
33. D. G. Vaughan *et al.*, in *Observations: Cryosphere*, T. F. Stocker *et al.*, Eds. (Cambridge Univ. Press, 2013), pp. 317–382.
34. M. van den Broeke *et al.*, *Science* **326**, 984–986 (2009).
35. W. Colgan *et al.*, *Ann. Glaciol.* **56**, 105–117 (2015).
36. H. J. Zwally, M. B. Giovinetto, M. A. Beckley, J. L. Saba, Antarctic and Greenland Drainage Systems (GSFC Cryospheric Sciences Laboratory, 2012); http://icesat4.gsfc.nasa.gov/cryo_data/ant_grn_drainage_systems.php.
37. I. Joughin, B. Smith, I. M. Howat, T. Scambos, T. Moon, *J. Glaciol.* **56**, 415–430 (2010).

ACKNOWLEDGMENTS

This work was supported by NSF (grants ARC 1107753, ARC 1108058, and ANT 0424589) and NASA (grants NNX12AB71G and NNX15AD55G). We thank the organizations (Center for Remote Sensing of Ice Sheets and Operation IceBridge) and innumerable individuals who aided in the collection and processing of radar data used in this study. Most of the early radar data used in this study were collected as part of NASA's Program for Arctic Regional Climate Assessment, which was initiated by Dr. Robert Thomas. We also thank I. Joughin for providing the updated surface-velocity composite. J.A.M., M.A.F., and G.A.C. designed this study; J.D.P. and S.P.G. contributed to the collection and processing of the radar data; J.A.M., W.T.C., M.A.F., M.M., and G.A.C. analyzed the results and wrote the manuscript; and all authors discussed the results and edited the manuscript. Data are archived at the National Snow and Ice Data Center (http://nsidc.org/data/rrrag4).

SUPPLEMENTARY MATERIALS

www.sciencemag.org/content/351/6273/590/suppl/DC1
Materials and Methods
Figs. S1 to S9
References (*38*–*46*)

23 March 2015; accepted 7 January 2016
10.1126/science.aab1702

Holocene deceleration of the Greenland Ice Sheet
Joseph A. MacGregor *et al.*
Science **351**, 590 (2016);
DOI: 10.1126/science.aab1702